4D Hyperspectral Photoacoustic Data Restoration with Reliability Analysis

Weihang Liao [1,2], Art Subpa-asa[2], Yinqiang Zheng[3], Imari Sato[1,2,3]

[1]Tokyo Institute of Technology, [2]National Institute of Informatics, [3]The University of Tokyo

liao.w.ac@m.titech.ac.jp, art@nii.ac.jp, yqzheng@ai.u-tokyo.ac.jp, imarik@nii.ac.jp

Abstract

Hyperspectral photoacoustic (HSPA) spectroscopy is an emerging bi-modal imaging technology that is able to show the wavelength-dependent absorption distribution of the interior of a 3D volume. However, HSPA devices have to scan an object exhaustively in the spatial and spectral domains; and the acquired data tend to suffer from complex noise. This time-consuming scanning process and noise severely affects the usability of HSPA. It is therefore critical to examine the feasibility of 4D HSPA data restoration from an incomplete and noisy observation. In this work, we present a data reliability analysis for the depth and spectral domain. On the basis of this analysis, we explore the inherent data correlations and develop a restoration algorithm to recover 4D HSPA cubes. Experiments on real data verify that the proposed method achieves satisfactory restoration results.

1. Introduction

Discovered in 1880 [4], the photoacoustic (PA) effect is a phenomenon in which materials emit acoustic signals under light irradiation. In the last few decades, photoacoustic imaging (PAI) [32] has emerged as a 3D imaging technology that combines light and ultrasound to form images. It has the advantages of both optical imaging (high optical contrast) and ultrasonic imaging (better penetration capability) [33] and thus is an alternative to X-ray exposure as a way to visualize the interiors of objects in a noninvasive manner. PAI uses light as an excitation source and an ultrasound sensor to detect sound waves generated by the optically excited targets. It can be used to analyze the properties and interior structure of a 3D volume [32, 33, 34, 37].

Thanks to the evolution of wavelength-tunable lasers, multispectral or hyperspectral photoacoustic (HSPA) imaging techniques have been developed. HSPA irradiates the material with different wavelengths of light and provides 4D data cubes, e.g. a 3D volume for each wavelength, as shown in Fig. 1. The amount of light absorbed by the material is determined by the spectral absorption coefficient of
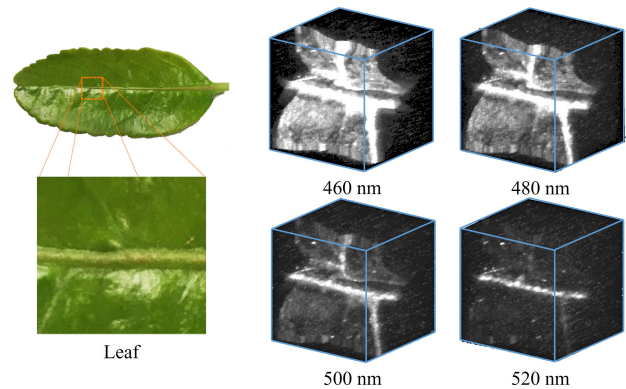

Figure 1. 4D HSPA data of leaf (rendering by KURUMI viewer [1]). The variance at each wavelength is clearly visible.

the material at each wavelength. HSPA has the capability of providing spectral absorbance information on the interiors of a target material, which support many tasks such as medical diagnosis, classification, and segmentation. Previous studies have shown that HSPA is promising in comprehensive clinical applications [35, 9, 20, 21].

A typical HSPA system is shown in Fig. 2, where an object is scanned by moving a wavelength-tunable laser and ultrasonic transducer along the surface of the object. There are two obstacles that severely limit practical use of HSPA: long acquisition time and complex noise. The data scanning process is time-consuming because it is performed exhaustively in the spatial and spectral domains. The ability to use fewer samples would speed up the data acquisition. HSPA also suffers from a very low signal to noise ratio (SNR) when the amount of received incident light is weak and when the spectral absorption coefficient is low. Thus, the SNR of HSPA should be adaptively enhanced. This issue motivated us to devise a method to restore full-grid, noise-free 4D HSPA data from incomplete and noisy observations.

In this paper, we first conduct a reliability analysis for different depths and spectrum wavelengths. Based on the analysis, we formulate the 4D HSPA restoration task as an optimization problem. We explore the data correlations, in-
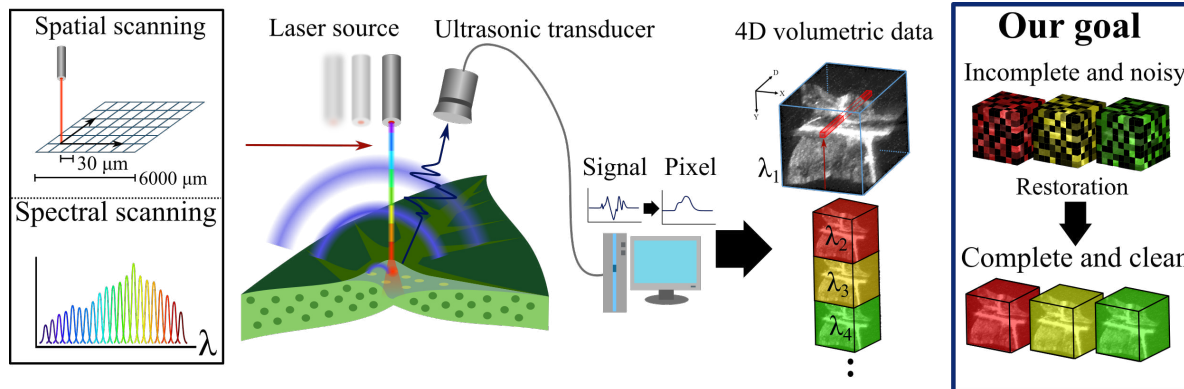
Figure 2. Scanning-based hyperspectral photoacoustic imaging system, whose scanning process is usually time-consuming.

cluding transform sparsity and local self-similarity, and represent them into regularization terms. Finally, we develop a numerical algorithm to reconstruct clear and high-quality data. Our contributions are summarized as follows:

1. For the first time, we consider the variance of the reliability of PA data and perform a depth and spectral reliability analysis.

2. On the basis of the results of the analysis, we propose an integral framework for 4D data restoration, in which data completion and denoising are simultaneously conducted.

2. Related Works

2.1. PA data completion

Various studies have used compressive sensing (CS) theory [11, 8] to complete PA data from a limited number of measurements and thereby accelerate the data acquisition. Provost and Lesage [29] proposed to use CS theory instead of the back-projection algorithm and achieved better performance than the simple pseudo-inverse on simulation data. Guo *et al.* [14] utilized CS theory to reduce the number of measurements and tested their method both on simulation data and in in vivo experiments. Liu *et al.* [24] used the alternating direction method to further accelerate the calculation. Arridge *et al.* [3] combined a model-based spatial sub-sampling scheme and total variation (TV) regularization to dramatically increase the acquisition speed. Haltmeier *et al.* [15] developed a sparsifying temporal transform and proposed a reconstruction algorithm with low complexity. The framework proposed in [16] jointly explores the sparsity of the original PA signal and the second-order derivative. Antholzer *et al.* [2] introduced a deep-learning method to solve the CS problem on PA data. Their method outperformed the default CS on simulation data, while it performed comparably to CS on real data due to the lack of training data.

All of the previous studies focused on 3D PA data completion; thus, they only studied sub-sampling in the spatial domain. This means there hasn't been enough research on 4D HSPA.

2.2. PA denoising

Some studies have tried to enhance the SNR or reduce the noise of 3D PA data. Telenkov and Mandelis [31] proposed to use chirped modulation waveforms to increase the SNR. Haq *et al.* [17] utilized K-means singular value decomposition to eliminate noise; it has been shown to perform better than Wiener or wavelet filtering. Zhang *et al.* [38] demonstrated that acoustic sub-aperture processing could be used to improve the SNR of PA data. Zhou *et al.* [41] proposed a denoising method combining empirical mode decomposition with conditional mutual information. There has also been a study on denoising of 4D multi-spectral PA data. Kazakeviciute *et al.* [19] treated the spectral bands as time series; they used an auto regressive model to estimate the noise and Wiener filter to perform denoising. However, they only explored the frontward spectrum correlation and ignored the backward correlation, because the auto regressive model only uses short wavelength data to predict the noise for long wavelength band.

The variance of the reliability of PA data was not well studied nor considered in previous works. Here, we propose a depth/spectral reliability analysis for HSPA data and enhance the SNR for different parts adaptively.

2.3. Low-rank representation

Low-rank representations have been proved to be effective in data restoration and are used in many applications. The key idea is to represent the data in a low-rank form and recover the underlying low-rank matrix from degraded observations [26]. Ji *et al.* [18] proposed to restore video by exploiting low-rank representations and sparsity. Zhang *et al.* [39] used low-rank matrix recovery to remove different kinds of noise and stripes from remote-sensing im-

ages. Dong *et al.* [10] proposed to use nonlocal low-rank regularization to recover MRI images. Fu *et al.* [12] explored spectral-spatial correlations via two low-rank terms and developed a reconstruction algorithm for coding-based HS imaging systems. Liu *et al.* [23, 22] proposed a system combining low-rank representations with CS theory and obtained 3D PA data with low sampling rates. In this study, we utilize low-rank representations for HSPA restoration.

In summary, most of the previous work focused on restoration of 3D data, while 4D HSPA restoration is a much more complicated issue, because: i) the signal amplitude is smaller due to the low energy conversion efficiency from light to sound [41]; ii) the observations are not equally reliable; it correlates with depth and spectral band; iii) it is challenging to observe sufficient PA effects from deep layers and bands with weak absorption. Thus, more constraints are needed for restoration. Below, we directly process 4D cubes to explore data correlations in different dimensions in HSPA.

3. Data Analysis

Let us first analyze the depth and spectral reliability of HSPA data. Unlike other high-dimensional data, such as video or hyper-spectral images, HSPA data have a special feature in which observations on different parts have dissimilar reliabilities depending on the absorbed light energy. This reliability correlates with both depth and spectral band; thus in this section, we discuss how to represent them.

3.1. Depth reliability analysis

During PA imaging, the object is irradiated by a laser pulse, and the absorbed light is converted into thermal energy, causing thermoelastic expansion. The expansion in turn causes a pressure change, which propagates as an acoustic wave. PAI utilizes ultrasonic transducer to capture this wave and translates it into an electric signal. The electrical signal is then amplified, digitized, and transformed by a computer into 3D volumetric data [32, 30].

The intensity of the PA signal is correlated with the amount of energy absorbed from the incident light. As light propagates in the material, its energy inevitably becomes weaker because of scattering and attenuation. Thus, objects deep inside the material absorb less light energy and consequently have a weaker signal intensity and lower SNR. Developers of PA imaging systems have reported that PA signal decays linearly with depth for a homogeneous material. This allows us to represent the depth-dependent PA-signal reliability by considering the depth of an interior point from the surface. For a small data patch $\mathcal{X}_d$ in depth d, its depth-dependent reliability can be described as

$$\gamma_{dep}(d) = \frac{I(d) - I_{min}}{I_{max} - I_{min}}, \tag{1}$$
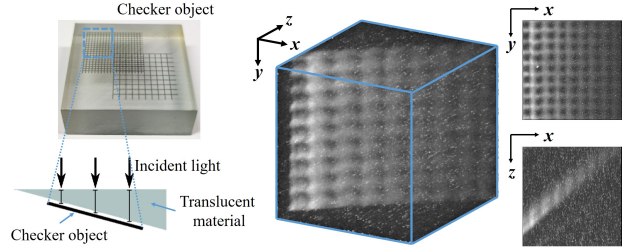

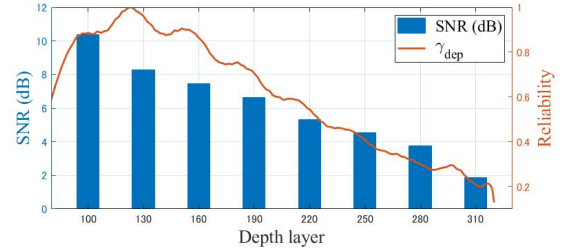Figure 3. 3D printed objects and PA data. The decay in signal intensity with depth can be seen.

Figure 4. Comparison of SNRs at different depths and predicted reliability.

where $I(d)$ is the average signal intensity in $\mathcal{X}_d$, and I_{max} and I_{min} are the maximum and minimum intensity of the whole PA cube, respectively. $\gamma_{dep} \in [0, 1]$, where 0 means a totally unreliable observation and 1 means a most reliable observation.

We verified the above depth-dependent reliability by examining the signal intensity of a 3D printed checker object. The checker pattern is installed at a tilt, covering with an translucent object, as shown in Fig. 3. It can be clearly observed that the lines in the deeper layer have a weaker signal intensity and suffer from more noise; the deepest line at the bottom is almost invisible. We uniformly selected eight depth layers and calculated their SNRs. Then we compared the SNRs with the proposed γ_{dep}, as shown in Fig. 4. We can see that γ_{dep} fits the tendency of the real SNR; this demonstrates the validity of the proposed depth reliability.

3.2. Spectral reliability analysis

PA imaging can provide spectral absorbance information on the interiors of target materials. Accordingly, another factor determining PA signal intensity is the spectral absorption of the material that determines the amount of light absorbed by that material. By considering the differences in PA signal intensities caused by differences in spectral absorption of the materials in the interior, we can represent the spectral reliability of the HSPA data captured at each wavelength length λ as

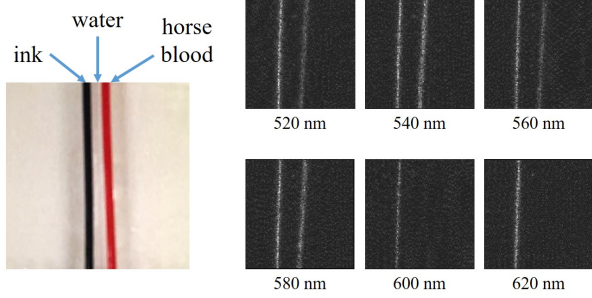$$\gamma_{spec}(\lambda) = \eta(\lambda) \cdot \phi(\lambda), \tag{2}$$

Figure 5. Three tubes containing ink, water, and horse blood. PA images acquired at different wavelengths.
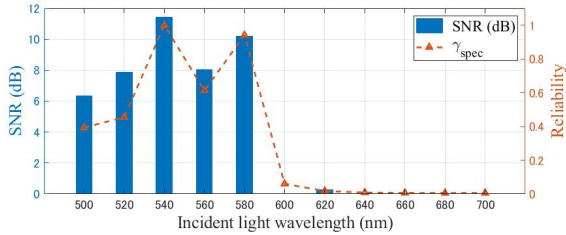

Figure 6. Comparison of SNR and predicted reliability for horse blood.

where $\eta(\cdot)$ is the laser emitter output energy function, and $\phi(\cdot)$ is the object's absorption spectrum. Moreover, as we did with depth reliability, we perform normalization on γ_{spec}, to make $\gamma_{spec} \in [0,1]$, where 0 means a totally unreliable band and 1 means a most reliable band.

We examined the validity of the proposed spectral reliability by measuring a scene consisting of three tubes of black ink, water, horse blood (Fig. 5). For this experiment, a laser light from 500 nm to 700 nm was used to irradiate the target scene at 20 nm intervals. We can see that the water tube is always invisible, because water is transparent, while the ink has constant light absorption at all wavelengths. Thus, the ink was captured in the PA images at all wavelengths. The blood tube has the strongest intensity at 540 nm, as the blood absorption spectrum has a peak here, and it is invisible beyond 600 nm. We calculated the SNR of the horse blood tube in each band and compared them with the proposed γ_{spec}, as shown in Fig. 6. We can see that the variation in γ_{spec} is similar to the tendency of the real SNR. This demonstrates the validity of the proposed spectral-reliability measure.

Finally, combining γ_{dep} and γ_{spec}, we define the total reliability as:

$$\gamma(d,\lambda) = c_1 \cdot \gamma_{dep}(d) \cdot \gamma_{spec}(\lambda) + c_2, \qquad (3)$$

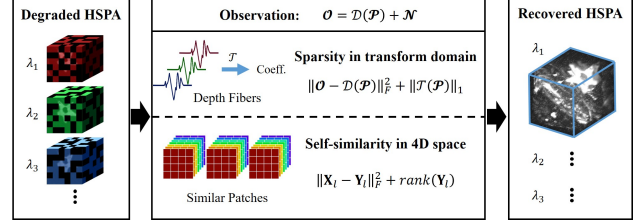where c_1 is the scaler and c_2 is the offset.

Figure 7. Overview of the proposed HSPA restoration method.

4. HSPA Data Restoration

First, we formulate the 4D HSPA restoration problem; then, we explore the data correlation globally and locally and incorporate the findings in regularization terms for optimization. Finally, we develop a numerical algorithm to solve the optimization problem. The overall framework is shown in Fig. 7.

4.1. Problem formulation

Consider HSPA data $\mathcal{P} \in \mathbb{R}^{n_1 \times n_2 \times n_3 \times n_4}$, where (n_1, n_2) is the spatial resolution, n_3 is the depth resolution, and n_4 is the spectral resolution. We formulate the degradation as:

$$\mathcal{O} = \mathcal{D}(\mathcal{P}) + \mathcal{N}, \qquad (4)$$

where $\mathcal{D}(\cdot)$ is a sub-sampling function, $\mathcal{N}$ is additive noise, $\mathcal{O}$ is the observation.

Our target is to restore clear, full-grid data $\mathcal{P}$ from a degraded observation $\mathcal{O}$. Obviously, this problem is ill-posed as there are many fewer observations than unknowns, and many observations are unreliable. To solve the optimization problem, we will explore the correlations between data and formulate them into an objective function.

4.2. Data constraints as regularization

We will explore two data constraints, i.e., global transform sparsity and local self-similarity. First, let us discuss the transform sparsity constraint. By specifying the spatial location (i,j) and spectral band λ, we can get a 1D vector $\mathbf{p}_{i,j,\lambda}$ along the depth direction. We call this 1D vector defined by fixing all indices but one a *Fiber*. According to the PA imaging mechanism, *Fiber* is a bipolar waveform signal [32]. We can always use an appropriate sparse transform for de-correlation [13]. Thus, we will impose the following constraint: *the depth Fiber should be sparse in a transform domain*. Popular sparse transforms include the Karhunen-Loeve transform (KLT), Fourier transform (FT), discrete cosine transform (DCT), etc. Here, we will use DCT for simplicity. Mathematically, sparsity can be achieved by minimizing the l_1 norm of the transformed coefficients:

$$\hat{\mathcal{P}} = \operatorname{argmin} \|\mathcal{T}_{dct}(\mathcal{P})\|_1, \ s.t. \|\mathcal{O} - \mathcal{D}(\mathcal{P})\|_F = 0, \quad (5)$$

where $\mathcal{T}_{dct}(\mathcal{P}) = \sum_i \sum_j \sum_\lambda \mathrm{dct}(\mathbf{p}_{i,j,\lambda})$ is the sum of DCTs of all depth *Fibers*.

Now, let us examine the local self-similarity constraint: *in a local region, a small patch should have a similar structure to its neighbor patches*. This similarity can be captured with a low-rank regularization term. Mathematically, we split the HSPA data $\mathcal{P}$ into several non-overlapping small patches $\{\mathcal{X}_1, \mathcal{X}_2, \cdots\}$; the size of each patch is $\mathcal{X} \in \mathbb{R}^{m_1 \times m_2 \times m_3 \times m_4}$. We will consider a patch $\mathcal{X}_l$ at location l and find the k nearest patches in a neighboring region in 4D space, denoted as $\{\Omega_{Nei}(\mathcal{X}_l)|\mathcal{X}_{N_1}, \mathcal{X}_{N_2}, \cdots, \mathcal{X}_{N_k}\}$. Note that we do not split the HSPA data into spatial and spectral domains; instead, we explore all of the data correlations simultaneously.

We reform the patch $\mathcal{X}_l$ into a vector $\mathbf{x}_l \in \mathbb{R}^M$, where $M = m_1 * m_2 * m_3 * m_4$. We perform the same vectorization on all neighboring patches in $\Omega_{Nei}(\mathcal{X}_l)$ and write them as a matrix $\mathbf{X}_l \in \mathbb{R}^{M \times (k+1)}$, where each row is a vectorized patch. This matrix has a low-rank structure in rows, because of the patches' self-similarity. Thus, we consider a noise model $\mathbf{X}_l = \mathbf{Y}_l + \mathbf{N}$, where $\mathbf{Y}_l$ is the desired noise-free low-rank matrix, and can be recovered as

$$\hat{\mathbf{Y}}_l = \arg\min \; rank(\mathbf{Y}_l), \; s.t. \|\mathbf{X}_l - \mathbf{Y}_l\|_F \le \sigma_N^2, \quad (6)$$

where σ_N^2 is the noise level.

4.3. Numerical algorithm

By writing equation (5), (6) in Lagrange function form and combining them with equation (4), we obtain the final objective function:

$$
\begin{aligned}
(\hat{\mathcal{P}}, \hat{\mathbf{Y}}) = &\arg\min \|\mathcal{O} - \mathcal{D}(\mathcal{P})\|_F^2 + \alpha\|\mathcal{T}_{dct}(\mathcal{P})\|_1 \\
&+ \sum_l \left[\gamma(d, \lambda)\|\mathbf{X}_l - \mathbf{Y}_l\|_F^2 + \beta \cdot rank(\mathbf{Y}_l) \right],
\end{aligned}
$$
$$(7)$$

where α and β are Lagrange multipliers and $\gamma(d, \lambda)$ is the adaptive reliability of each local patch, as defined in section 3.2. This objective function contains two parts (global transform sparsity and local self-similarity), and we solve them sequentially.

Step 1: for global transform sparsity, we denote $\mathcal{Q} = \mathcal{T}_{dct}(\mathcal{P})$; thus, equation (5) becomes

$$\hat{\mathcal{Q}} = \arg\min \frac{1}{2}\|\mathcal{O} - \mathcal{D}(\mathcal{T}_{idct}(\mathcal{Q}))\|_F^2 + \frac{\alpha}{2}\|\mathcal{Q}\|_1, \quad (8)$$

where $\mathcal{T}_{idct}(\cdot)$ is the sum of inverse DCTs of all depth *Fibers*. Equation (8) is a typical Lasso problem; we solve it by using the alternating direction method of multipliers (ADMM) [5]. Consequently, we get the intermediate result $\tilde{\mathcal{P}} = \mathcal{T}_{idct}(\hat{\mathcal{Q}})$.

Step 2: we split $\tilde{\mathcal{P}}$ into small patches and calculate the reliability for each patch based on their depth and spectral

band, as defined in equation (3). We write out the low-rank matrix and local self-similarity constraint equation for each patch, as described in the previous sub-section. The rank term in equation (6) is non-convex and NP-hard; a common solution is to approximate it using the nuclear norm [7]. Thus, we rewrite equation (6) as

$$\hat{\mathbf{Y}} = \arg\min \frac{1}{2}\|\mathbf{X} - \mathbf{Y}\|_F^2 + \frac{\beta}{2\gamma}\|\mathbf{Y}\|_*, \quad (9)$$

where $\|\cdot\|_*$ is the nuclear norm. According to [6], equation (9) can be optimized as

$$\hat{\mathbf{Y}} = \mathbf{U}\mathcal{S}(\mathbf{\Sigma}, \frac{\beta}{2\gamma})\mathbf{V}^\top, \mathcal{S}(\mathbf{\Sigma}, \frac{\beta}{2\gamma}) = \mathrm{diag}\left\{ \left(\sigma_X - \frac{\beta}{2\gamma}\right)_+ \right\},$$
$$(10)$$

where $\mathbf{U}\mathbf{\Sigma}\mathbf{V}^\top$ is the singular value decomposition of $\mathbf{X}$, and σ_X are the singular values. $\mathcal{S}(\cdot)$ is the singular value shrinkage operator, $(a)_+ = \max(0, a)$.

Step 3:, we reconstruct clear small patches $\hat{\mathcal{X}}$ from $\hat{\mathbf{Y}}$ and combine them to form the final restoration result $\hat{\mathcal{P}}$.

5. Experimental Results

First, we will describe the dataset used in the experiments and the reference for the performance evaluation. Then, we will present qualitative and quantitative results on the proposed restoration method and verify the depth and spectral reliabilities.

5.1. Data set

Our dataset consists of two types of data: 4D HSPA data and high-resolution blood vessel PA data. The HSPA data include 'Leaf', 'Tube', and 'Banana'. They were captured using a photoacoustic microscope machine (ADVANTEST, Hadatomo™ Z WEL5200) connected to a wavelength tunable laser emitter (Japan Laser, Opolette HR 355). We measured a 6 mm^2 area with a 30 μm scanning interval over 1280 time steps. The resulting 4D volumetric data had a resolution of $200 \times 200 \times 1280 \times$ bands. For Leaf and Banana, we uniformly measured 9 bands ranging from 420 nm to 580 nm. For Tube, we uniformly measured 11 bands ranging from 500 nm to 700 nm. The entire HSPA data are shown in the supplementary material.

The blood vessel PA data consisted of 'Hand' and 'Leg'. They were captured by the PAI-05 system proposed in [28]. The blood vessel PA is provided at a higher resolution for large body parts by fusing several PA data. Because of scanning time limitations, 'Hand' and 'Leg' consist of only single-band PA data. The wavelength of the incident light was 797 nm, which is the isosbestic point of oxyhemoglobin and de-oxygenated hemoglobin [28]. The full resolution is $2480 \times 1760 \times 160$ for Hand, and $2176 \times 1440 \times 256$ for Leg.

5.2. Evaluation reference

The major challenge of evaluating the performance of PA restoration algorithms is the lack of a reliable baseline. The original data contains noise, and typical techniques such as averaging over multiple shots are difficult to perform because of mechanical misalignment between shots. Thus we first acquire a noise-removed full-grid data by considering local self-similarity and data reliability. This clear data will be later used as a reference in the following evaluations.

Here we examined the validity of noise-removed full-grid reference using a simple scene consisting of a single opaque plane. In this care, only a point (x, y, z) on the plane should exhibit a strong PA signal. From this, we fitted a plane by applying the least squares method and calculated the ground-truth surface locations $(x, y, z)_{gt}$. Then we compared locations of maximum intensity points from the original noisy observation and our reference data with $(x, y, z)_{gt}$. We captured an opaque plane with five different orientations. The average sum of squares of errors (SSE) for the noisy observations was 114.9421, while the average SSE for our reference was only 2.7237, which demonstrates the validity of our reference data. The full error matrices for each orientation are in the supplementary material.

5.3. Performance evaluation and comparison

We quantitatively and qualitatively evaluated i) the overall performance of our method, ii) the effectiveness of depth reliability, and iii) the effectiveness of spectral reliability.

For the quantitative evaluation, the most widely used metrics are the peak signal-to-noise ratio (PSNR) and structural similarity (SSIM) [36]. These metrics were originally designed for 2D gray-scale images, while the PA data has more dimensions and contains negative values. Thus, we applied a Hilbert transform and re-scaled the PA data to [0, 255]; then, we calculated the quality metrics on each 2D slice by fixing the depth and spectral band. We used the average value among all slices for the evaluation; larger numbers indicate better restoration quality.

5.3.1 Restoration method evaluation

We verified our methods on incomplete and noisy observations, which were randomly sub-sampled from the original data. We evaluated the restoration quality against those of other approaches, including the default compressive sensing (CS) algorithm, CS with a Wiener filter (CS + Wiener), and CS with partially known support (CS-PKS) algorithm [27]. We also compared with sophisticated restoration techniques that are not originally developed for PA data, including BM4D[25] and SMF-LRTC[40]. The visualizations for restoration results are shown in Fig. 8 (visualizations of Tube and Banana are in the supplementary material). We visualize a part of original data (480 nm for Leaf, palm for

Hand, ankle for Leg) in (a), and show 2D slices for reference data and different approaches in (b-g). The quantitative metrics are listed in Table 1, the results show that our method outperforms the others with or without reliability.

The default CS result is very noisy and has the lowest PSNR and SSIM. This is because CS utilizes the basis pursuit algorithm as the solver, which doesn't take noise into consideration. CS + Wiener, CS + BM4D, and SMF-LRTC outperformed default CS, but still had obvious defects. CS-PKS over-smoothed the edge and lost some details, because of the total variation term in the objective function, which optimizes the global smoothness in the spatial domain. Our method produced a noise-free and detailed restoration; the visual quality was close to that of the reference data. Quantitatively, our method had the highest PSNR and SSIM for almost all data and all sampling ratios. This is because our method does not split the high-dimensional PA data into spatial and depth domains; instead it allowed all of the data correlations to be explored simultaneously.

We further visualize the restoration result of our method on other portions of Hand data, as shown in Fig. 9. A satisfactory and stable restoration performance can be observed for them.

5.3.2 Depth reliability verification

We verified the depth reliability by observing two different depth layers of Hand and Leg, as shown in Fig. 10, where the first row shows a shallow layer and the second row shows a deep layer. The reference data, restoration results with reliability (marked in red), and results without reliability (marked in green) are in columns (a), (b), (d) and (e), respectively. Utilizing the reference data as a baseline, we calculated the absolute error map of the results with and without reliability, as shown in column (c) and (f). It can be seen that for the shallow layer, the results with and without reliability have similar restoration quality. On the other hand, for the deep layer where the signal intensity is low, reliability obviously improves the performance. These results demonstrate the effectiveness of depth reliability.

5.3.3 Spectral reliability verification

The PSNR and SSIM results across all spectral bands are plotted in Fig. 11. For Banana, our method achieve a similar degree of improvement across all bands, as the data has strong signal intensity due to the consistent high absorptions. For Leaf in wavelengths with high absorptions (420 to 480 nm), our method produces a marginal improvement over other approaches. On the other hand, for wavelengths with low absorptions (500 to 580 nm), the data have much lower signal intensity. Our method with reliability has higher PSNR, because it adaptively adjusts the optimization
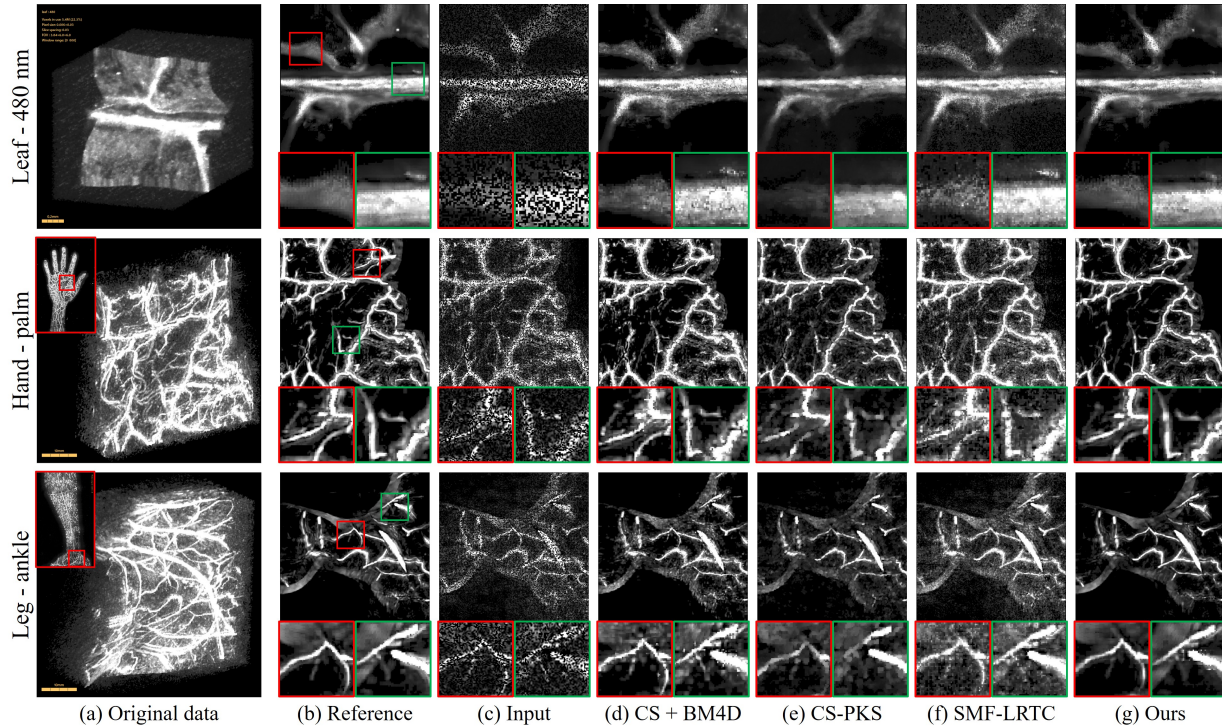
Figure 8. The visualization of restoration results by different methods on 50% sampled data.

Table 1. The quantitative results for different methods

Sample Ratio	Method	Leaf		Tube		Banana		Hand - palm		Leg - ankle	
		PSNR	SSIM	PSNR	SSIM	PSNR	SSIM	PSNR	SSIM	PSNR	SSIM
0.7	default CS	31.78	0.1480	31.18	0.1130	34.80	0.1838	37.46	0.2119	39.48	0.3173
	CS + Wiener	36.38	0.2366	38.63	0.1885	35.35	0.2130	40.44	0.2559	42.33	0.3646
	CS + BM4D	37.68	0.2204	39.02	0.1465	36.11	0.2534	41.23	0.2701	43.20	0.3846
	CS-PKS	35.84	0.1650	37.73	0.0877	35.79	0.2925	40.10	0.2577	41.98	0.3721
	SMF-LRTC	32.51	0.1713	31.60	0.1333	37.36	0.2400	37.76	0.2138	39.86	0.3222
	Ours w/o reliab.	37.77	0.5094	38.92	0.4604	39.27	0.4081	42.94	0.2909	45.84	0.4398
	Ours w/ reliab.	**44.35**	**0.5528**	**45.86**	**0.4989**	**42.75**	**0.8129**	**53.01**	**0.9695**	**55.97**	**0.9784**
0.5	default CS	31.58	0.1277	31.71	0.0909	32.27	0.1277	37.47	0.2094	39.43	0.3123
	CS + Wiener	35.50	0.1971	38.92	0.1508	31.83	0.1383	39.93	0.2532	41.77	0.3584
	CS + BM4D	36.51	0.1902	39.45	0.1231	32.06	0.1500	40.91	0.2769	42.82	0.3856
	CS-PKS	34.92	0.1425	38.63	0.0760	34.57	0.2622	39.57	0.2534	41.33	0.3612
	SMF-LRTC	32.84	0.1626	32.43	0.1254	37.24	0.2307	38.08	0.2145	40.26	0.3253
	Ours w/o reliab.	36.63	0.3840	38.93	0.3273	37.15	0.3855	42.72	0.3013	45.25	0.4437
	Ours w/ reliab.	**40.13**	**0.4148**	**43.33**	**0.3577**	**38.45**	**0.6523**	**46.75**	**0.8856**	**49.19**	**0.9033**
0.3	default CS	31.13	0.0889	32.35	0.0630	29.54	0.0691	36.75	0.1891	38.58	0.2797
	CS + Wiener	34.03	0.1419	38.66	0.1015	29.03	0.0714	38.36	0.2335	40.08	0.3226
	CS + BM4D	34.82	0.1418	39.35	0.0889	29.23	0.0858	39.05	0.2642	40.89	0.3564
	CS-PKS	32.94	0.1049	38.64	0.0581	32.50	0.2037	37.28	0.2002	39.05	0.2910
	SMF-LRTC	32.99	0.1476	33.62	0.1152	**36.55**	0.2117	38.17	0.2110	40.49	0.3238
	Ours w/o reliab.	35.02	0.2682	38.82	0.2155	34.66	0.3254	40.69	0.3056	42.73	0.4295
	Ours w/ reliab.	**35.99**	**0.2870**	**40.41**	**0.2398**	34.79	**0.4379**	**41.13**	**0.6879**	**43.51**	**0.7101**

weight according to the reliability of the prior knowledge. This result verifies the effectiveness of spectral reliability.

6. Conclusions

We studied the hyperspectral photoacoustic (HSPA) data restoration problem. We discussed the variance in reliabil-ity at different depths and in different spectral bands. On the basis of the reliability analysis, we proposed a framework to reconstruct clear, high-quality HSPA data from incomplete, noisy observations. The correlations of the data in different dimensions can be explored simultaneously by using low-rank representations and sparsity regularization. We veri-fied our method on captured HSPA data and blood vessel
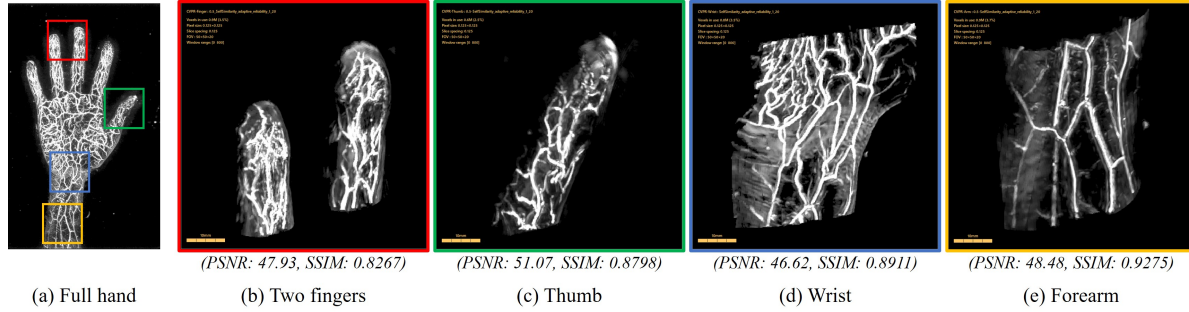
(a) Full hand   (b) Two fingers   (c) Thumb   (d) Wrist   (e) Forearm

(PSNR: 47.93, SSIM: 0.8267)   *(PSNR: 51.07, SSIM: 0.8798)*   *(PSNR: 46.62, SSIM: 0.8911)*   *(PSNR: 48.48, SSIM: 0.9275)*

Figure 9. The visualization of restoration results for different portions of 50% sampled Hand data.

(a) Reference - Hand   (b) Restoration   (c) Error map   (d) Reference - Leg   (e) Restoration   (f) Error map
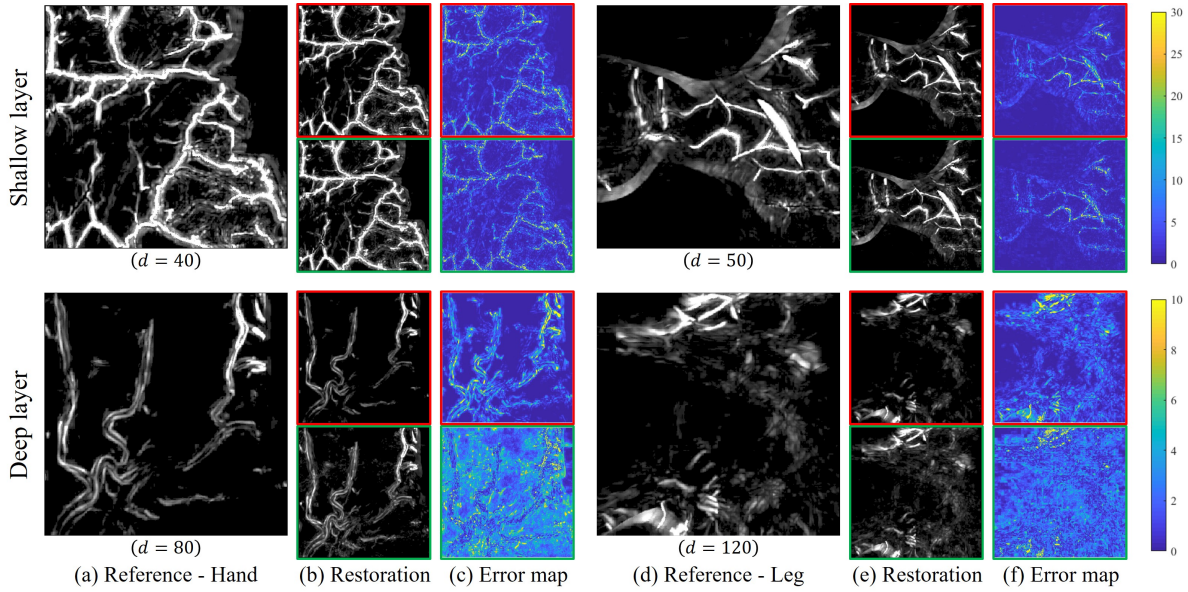
Figure 10. Results of restoration on 50% sampled data at different depths (Hand and Leg). The results with reliability are marked in red, and results without reliability are marked in green.

(a) Leaf - PSNR result   (b) Leaf - SSIM result   (c) Banana - PSNR result   (d) Banana - SSIM result
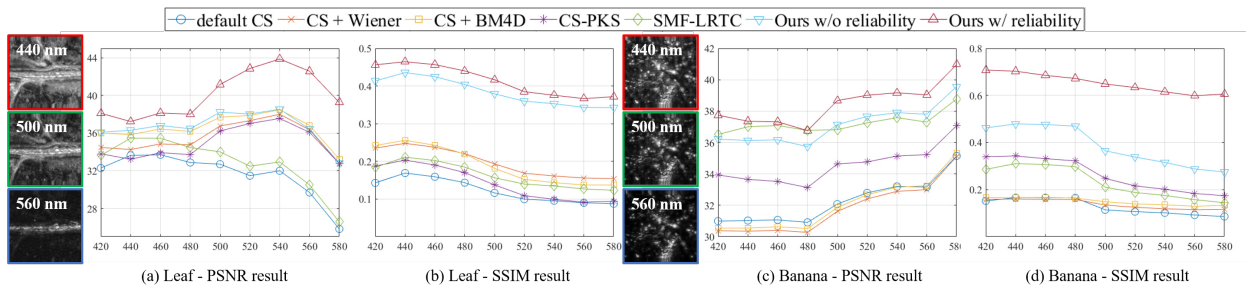
Figure 11. Quality of restoration on 50% sampled data across spectral bands (Leaf and Banana).

PA data. The results show that our method has satisfactory restoration performance.

References

[1] Kyoto university rapid and universal mip imager. `https://www.kuhp.kyoto-u.ac.jp/~diag_rad/intro/tech/kurumi.html#KURUMI_EN`. Accessed: 2020-03-05. 1

[2] Stephan Antholzer, Johannes Schwab, Johnnes Bauer-Marschallinger, Peter Burgholzer, and Markus Haltmeier. Nett regularization for compressed sensing photoacoustic tomography. In *Photons Plus Ultrasound: Imaging and Sensing 2019*, volume 10878, page 108783B. International Society for Optics and Photonics, 2019. 2

[3] Simon Arridge, Paul Beard, Marta Betcke, Ben Cox, Nam Huynh, Felix Lucka, Olumide Ogunlade, and Edward Zhang. Accelerated high-resolution photoacoustic tomography via compressed sensing. *arXiv preprint arXiv:1605.00133*, 2016. 2

[4] Alexander Graham Bell. Upon the production and reproduction of sound by light. *Journal of the Society of Telegraph Engineers*, 9(34):404–426, 1880. 1

[5] Stephen Boyd, Neal Parikh, Eric Chu, Borja Peleato, Jonathan Eckstein, et al. Distributed optimization and statistical learning via the alternating direction method of multipliers. *Foundations and Trends® in Machine learning*, 3(1):1–122, 2011. 5

[6] Jian-Feng Cai, Emmanuel J Candès, and Zuowei Shen. A singular value thresholding algorithm for matrix completion. *SIAM Journal on optimization*, 20(4):1956–1982, 2010. 5

[7] Emmanuel J Candès and Benjamin Recht. Exact matrix completion via convex optimization. *Foundations of Computational mathematics*, 9(6):717, 2009. 5

[8] Emmanuel J Candès and Michael B Wakin. An introduction to compressive sampling. *IEEE signal processing magazine*, 25(2):21–30, 2008. 2

[9] Yingchun Cao, Ayeeshik Kole, Lu Lan, Pu Wang, Jie Hui, Michael Sturek, and Ji-Xin Cheng. Spectral analysis assisted photoacoustic imaging for lipid composition differentiation. *Photoacoustics*, 7:12–19, 2017. 1

[10] Weisheng Dong, Guangming Shi, Xin Li, Yi Ma, and Feng Huang. Compressive sensing via nonlocal low-rank regularization. *IEEE Transactions on Image Processing*, 23(8):3618–3632, 2014. 3

[11] David L Donoho. Compressed sensing. *IEEE Transactions on information theory*, 52(4):1289–1306, 2006. 2

[12] Ying Fu, Yinqiang Zheng, Imari Sato, and Yoichi Sato. Exploiting spectral-spatial correlation for coded hyperspectral image restoration. In *Proceedings of the IEEE Conference on Computer Vision and Pattern Recognition*, pages 3727–3736, 2016. 3

[13] Roger G Ghanem and Pol D Spanos. *Stochastic finite elements: a spectral approach*. Courier Corporation, 2003. 4

[14] Zijian Guo, Changhui Li, Liang Song, and Lihong V Wang. Compressed sensing in photoacoustic tomography in vivo. *Journal of biomedical optics*, 15(2):021311, 2010. 2

[15] Markus Haltmeier, Thomas Berer, Sunghwan Moon, and Peter Burgholzer. Compressed sensing and sparsity in photoacoustic tomography. *Journal of Optics*, 18(11):114004, 2016. 2

[16] Markus Haltmeier, Michael Sandbichler, Thomas Berer, Johannes Bauer-Marschallinger, Peter Burgholzer, and Linh Nguyen. A sparsification and reconstruction strategy for compressed sensing photoacoustic tomography. *The Journal of the Acoustical Society of America*, 143(6):3838–3848, 2018. 2

[17] Israr Ul Haq, Ryo Nagaoka, Syahril Siregar, and Yoshifumi Saijo. Sparse-representation-based denoising of photoacoustic images. *Biomedical Physics & Engineering Express*, 3(4):045014, 2017. 2

[18] Hui Ji, Sibin Huang, Zuowei Shen, and Yuhong Xu. Robust video restoration by joint sparse and low rank matrix approximation. *SIAM Journal on Imaging Sciences*, 4(4):1122–1142, 2011. 2

[19] Agne Kazakeviciute, Chris Jun Hui Ho, and Malini Olivo. Multispectral photoacoustic imaging artifact removal and denoising using time series model-based spectral noise estimation. *IEEE transactions on medical imaging*, 35(9):2151–2163, 2016. 2

[20] Hoong-Ta Lim and Vadakke Matham Murukeshan. Hyperspectral photoacoustic spectroscopy of highly-absorbing samples for diagnostic ocular imaging applications. *International Journal of Optomechatronics*, 11(1):36–46, 2017. 1

[21] Ning Liu, Sihua Yang, and Da Xing. Photoacoustic and hyperspectral dual-modality endoscope. *Optics letters*, 43(1):138–141, 2018. 1

[22] Ting Liu, Mingjian Sun, Yang Liu, Depeng Hu, Yiming Ma, Liyong Ma, and Naizhang Feng. Admm based low-rank and sparse matrix recovery method for sparse photoacoustic microscopy. *Biomedical Signal Processing and Control*, 52:14–22, 2019. 3

[23] Ting Liu, Mingjian Sun, Jing Meng, Zhenghua Wu, Yi Shen, and Naizhang Feng. Compressive sampling photoacoustic microscope system based on low rank matrix completion. *Biomedical Signal Processing and Control*, 26:58–63, 2016. 3

[24] Xueyan Liu, Dong Peng, Wei Guo, Xibo Ma, Xin Yang, and Jie Tian. Compressed sensing photoacoustic imaging based on fast alternating direction algorithm. *International journal of biomedical imaging*, 2012, 2012. 2

[25] Matteo Maggioni, Vladimir Katkovnik, Karen Egiazarian, and Alessandro Foi. Nonlocal transform-domain filter for volumetric data denoising and reconstruction. *IEEE transactions on image processing*, 22(1):119–133, 2012. 6

[26] Ivan Markovsky and KONSTANTIN Usevich. *Low rank approximation*. Springer, 2012. 2

[27] Jing Meng, Lihong V Wang, Leslie Ying, Dong Liang, and Liang Song. Compressed-sensing photoacoustic computed tomography in vivo with partially known support. *Optics Express*, 20(15):16510–16523, 2012. 6

[28] Kenichi Nagae, Yasufumi Asao, Yoshiaki Sudo, Naoyuki Murayama, Yuusuke Tanaka, Katsumi Ohira, Yoshihiro Ishida, Atsushi Otsuka, Yoshiaki Matsumoto, Susumu Saito, et al. Real-time 3d photoacoustic visualization system with a wide field of view for imaging human limbs. *F1000Research*, 7, 2018. 5

[29] Jean Provost and Frédéric Lesage. The application of compressed sensing for photo-acoustic tomography. *IEEE transactions on medical imaging*, 28(4):585–594, 2008. 2

[30] Allan Rosencwaig and Allen Gersho. Theory of the photoacoustic effect with solids. *Journal of Applied Physics*, 47(1):64–69, 1976. 3

[31] Sergey Telenkov and Andreas Mandelis. Signal-to-noise analysis of biomedical photoacoustic measurements in time and frequency domains. *Review of Scientific Instruments*, 81(12):124901, 2010. 2

[32] Lihong V Wang. Tutorial on photoacoustic microscopy and computed tomography. *IEEE Journal of Selected Topics in Quantum Electronics*, 14(1):171–179, 2008. 1, 3, 4

[33] Lihong V Wang and Song Hu. Photoacoustic tomography: in vivo imaging from organelles to organs. *science*, 335(6075):1458–1462, 2012. 1

[34] Lihong V Wang and Junjie Yao. A practical guide to photoacoustic tomography in the life sciences. *Nature methods*, 13(8):627, 2016. 1

[35] Pu Wang, Ping Wang, Han-Wei Wang, and Ji-Xin Cheng. Hyperspectral vibrational photoacoustic imaging of lipids and collagen. In *Photons Plus Ultrasound: Imaging and Sensing 2012*, volume 8223, page 82231I. International Society for Optics and Photonics, 2012. 1

[36] Zhou Wang, Alan C Bovik, Hamid R Sheikh, and Eero P Simoncelli. Image quality assessment: from error visibility to structural similarity. *IEEE transactions on image processing*, 13(4):600–612, 2004. 6

[37] Minghua Xu and Lihong V Wang. Photoacoustic imaging in biomedicine. *Review of scientific instruments*, 77(4):041101, 2006. 1

[38] Ge Zhang, Bingxue Wang, Antonio Stanziola, Anant Shah, Jeffrey Bamber, and Meng-Xing Tang. High signal-to-noise ratio contrast-enhanced photoacoustic imaging using acoustic sub-aperture processing and spatiotemporal filtering. In *2019 IEEE International Ultrasonics Symposium (IUS)*, pages 494–497. IEEE, 2019. 2

[39] Hongyan Zhang, Wei He, Liangpei Zhang, Huanfeng Shen, and Qiangqiang Yuan. Hyperspectral image restoration using low-rank matrix recovery. *IEEE Transactions on Geoscience and Remote Sensing*, 52(8):4729–4743, 2013. 2

[40] Yu-Bang Zheng, Ting-Zhu Huang, Teng-Yu Ji, Xi-Le Zhao, Tai-Xiang Jiang, and Tian-Hui Ma. Low-rank tensor completion via smooth matrix factorization. *Applied Mathematical Modelling*, 70:677–695, 2019. 6

[41] Meng Zhou, Haibo Xia, Hongtao Zhong, Jiayao Zhang, and Fei Gao. A noise reduction method for photoacoustic imaging in vivo based on emd and conditional mutual information. *IEEE Photonics Journal*, 11(1):1–10, 2019. 2, 3